

## Airborne Measurements of Mesoscale Divergence at High Latitudes during HALO–(AC)3

Paulus, Fiona M.; Karalis, Michail; George, Geet; Svensson, Gunilla; Wendisch, Manfred; Neggers, Roel A.J.

**DOI**

[10.1175/JAS-D-24-0034.1](https://doi.org/10.1175/JAS-D-24-0034.1)

**Publication date**

2024

**Document Version**

Final published version

**Published in**

Journal of the Atmospheric Sciences

**Citation (APA)**

Paulus, F. M., Karalis, M., George, G., Svensson, G., Wendisch, M., & Neggers, R. A. J. (2024). Airborne Measurements of Mesoscale Divergence at High Latitudes during HALO–(AC)3. *Journal of the Atmospheric Sciences*, 81(12), 2051-2067. <https://doi.org/10.1175/JAS-D-24-0034.1>

**Important note**

To cite this publication, please use the final published version (if applicable).  
Please check the document version above.

**Copyright**

Other than for strictly personal use, it is not permitted to download, forward or distribute the text or part of it, without the consent of the author(s) and/or copyright holder(s), unless the work is under an open content license such as Creative Commons.

**Takedown policy**

Please contact us and provide details if you believe this document breaches copyrights.  
We will remove access to the work immediately and investigate your claim.

## Airborne Measurements of Mesoscale Divergence at High Latitudes during HALO-(AC)<sup>3</sup>

FIONA M. PAULUS<sup></sup>,<sup>a</sup> MICHAEL KARALIS,<sup>b</sup> GEET GEORGE,<sup>c,d</sup> GUNILLA SVENSSON,<sup>b,e</sup> MANFRED WENDISCH,<sup>f</sup> AND ROEL A. J. NEGGERS<sup>a</sup>

<sup>a</sup> *Institute for Geophysics and Meteorology, University of Cologne, Cologne, Germany*

<sup>b</sup> *Department of Meteorology and Bolin Centre for Climate Research, Stockholm University, Stockholm, Sweden*

<sup>c</sup> *Max Planck Institute for Meteorology, Hamburg, Germany*

<sup>d</sup> *Delft University of Technology, Delft, Netherlands*

<sup>e</sup> *Department of Engineering Mechanics, KTH Royal Institute of Technology, FLOW, Stockholm, Sweden*

<sup>f</sup> *Leipzig Institute for Meteorology, University Leipzig, Leipzig, Germany*

(Manuscript received 4 March 2024, in final form 1 August 2024, accepted 2 August 2024)

**ABSTRACT:** Boundary layer cloud transformations at high latitudes play a key role for the Arctic climate and are partially controlled by large-scale dynamics such as subsidence. While measuring large-scale and mesoscale divergence on spatial scales on the order of 100 km has proven notoriously difficult, recent airborne campaigns in the subtropics have successfully applied measurement techniques using multiple dropsonde releases in circular flight patterns. In this paper, it is shown that this method can also be effectively applied at high latitudes, in spite of the considerable differences in atmospheric dynamics compared to the subtropics. To show the applicability, data collected during the airborne High Altitude and Long Range Research Aircraft–Transregional Collaborative Research Center TRR 172–Arctic Amplification: Climate Relevant Atmospheric and Surface Processes and Feedback Mechanisms [HALO-(AC)<sup>3</sup>] field campaign near Svalbard in spring 2022 were analyzed, where several flight patterns involving multiple dropsonde launches were realized by two aircraft. This study presents a first overview of the results. We find that the method indeed yields reliable estimates of mesoscale gradients in the Arctic, producing robust vertical profiles of horizontal divergence and, consequently, subsidence. Sensitivity to aspects of the method is investigated, including dependence on sampling area and the divergence calculation.

**SIGNIFICANCE STATEMENT:** The aim of this work is to report encouraging results with a recently proposed aircraft-based method for measuring mesoscale vertical motions at high latitudes. Dropsonde data from the recent High Altitude and Long Range Research Aircraft–Transregional Collaborative Research Center TRR 172–Arctic Amplification: Climate Relevant Atmospheric and Surface Processes and Feedback Mechanisms [HALO-(AC)<sup>3</sup>] campaign are used for this purpose. The method has so far mainly been applied at subtropical to midlatitudes, but not in the Arctic, where the weather and climate conditions are very different. Gaining insight is significant because vertical winds play a key role in the Arctic climate system, including airmass transformations and the behavior of clouds and precipitation. The results motivate the use of the measured vertical winds in follow-up studies with process models.

**KEYWORDS:** Arctic; Convergence/divergence; Dropsondes

### 1. Introduction

The accurate representation of vertical motion, including divergence and subsidence, is essential for model studies, particularly to represent the boundary layer and study clouds. Divergence and related vertical motions (including subsidence) change the vertical structure of the atmosphere, influencing thermal stability and relative humidity, which in turn affect radiation and cloud dynamics. Neggers et al. (2019) established a direct link between subsidence and the life cycle of low-level clouds in the Arctic, where strong and sudden subsidence events were responsible for cloud collapses. This discovery, based on Lagrangian large-eddy simulation (LES) experiments

of transitioning warm airmass intrusions into the high Arctic, holds significant implications for the local energy budgets in the Arctic.

Therefore, the study of subsidence is of premier importance. However, measuring subsidence presents a classic challenge in meteorology. The small signal and considerable fluctuation of vertical motion pose obstacles to direct observation. This challenge has led to the development of various methods to estimate and quantify subsidence. Lenschow et al. (1999) pioneered methods to quantify horizontal divergence through aircraft-based measurements, while Mapes and Lin (2005) developed a method to derive divergence, and thereby subsidence, using ground-based Doppler radar observations. These methods rely on mass conservation for deriving the divergence. While surface-based methods have been used widely to measure subsidence (Mapes et al. 2003; Mapes and Lin 2005; Li et al. 2018), they can be challenging to apply in the Arctic, particularly in the central Arctic region. The remote and harsh conditions of the Arctic, along with limited

 Denotes content that is immediately available upon publication as open access.

*Corresponding author:* Fiona M. Paulus, fpaulus@uni-koeln.de

DOI: 10.1175/JAS-D-24-0034.1

© 2024 American Meteorological Society. This published article is licensed under the terms of the default AMS reuse license. For information regarding reuse of this content and general copyright information, consult the AMS Copyright Policy ([www.ametsoc.org/PUBSReuseLicenses](http://www.ametsoc.org/PUBSReuseLicenses)).

accessibility, imply serious difficulties for deploying and maintaining land-based measurement systems. As a result, aircraft-based methods offer a viable alternative for obtaining subsidence information in these challenging environments.

Recent advancements in atmospheric research have introduced a new technique for measuring vertical motion, through dropsondes released along horizontal, circular flight patterns by aircraft (Bony and Stevens 2019), inspired by techniques based on Lenschow et al. (2007). Notably, campaigns like the Next Generation Remote Sensing for Validation Studies (NARVAL2) (Bony and Stevens 2019) and Elucidating the Role of Clouds–Circulation Coupling in Climate (EUREC<sup>4</sup>A) (Stevens et al. 2021) have leveraged the High Altitude and Long-Range Research Aircraft (HALO) to execute these horizontal circles in the subtropics. While the method has already shown promise in subtropical regions (Bony and Stevens 2019; George et al. 2021) and cold-air outbreaks in the western North Atlantic Ocean (Li et al. 2022), its applicability to the Arctic cannot be assumed a priori. The theoretical suitability of this method for Arctic studies opens novel pathways to probe the complexities of vertical motion and its implications. The distinct atmospheric conditions in the Arctic, however, pose unique challenges that differ from those encountered in subtropical areas. The Rossby radius and time scale of deformation decrease with latitude, causing the dynamical features in the Arctic to be more transient and spatially constrained. This calls into question the soundness of the stationarity assumption necessary for this observational framework, as well as the representativity of the column measurements for the general divergence fields, which were previously established for the subtropics (Bony and Stevens 2019). Therefore, exploring the viability of this method in the Arctic context is of paramount importance, as it holds the potential to unravel crucial insights into subsidence dynamics and their implications in high-latitude regions.

The HALO–Transregional Collaborative Research Center TRR 172–Arctic Amplification: Climate Relevant Atmospheric and Surface Processes and Feedback Mechanisms [HALO–(AC)<sup>3</sup>] campaign in March and April 2022 was partly designed to evaluate the method within the Arctic context. The central goals of the campaign include the investigation of key aspects of atmospheric circulation such as airmass transformations and their implications for climate dynamics in the Arctic through quasi-Lagrangian observations (Wendisch et al. 2021). One of the primary objectives was to study the transformations of air masses during warm-air intrusions and cold-air outbreaks in the Arctic region. A key focus of the campaign involved flying mesoscale [ $\mathcal{O}(100)$  km, 1 h] horizontal circles with HALO, during which dropsondes are released at regular intervals along the circle. These circles can capture the area-averaged atmospheric divergence and subsidence, allowing further investigations on airmass dynamics.

This study undertakes a dual-pronged investigation with the primary goals of determining the effectiveness of the horizontal circle method and comprehensively substantiating the feasibility of employing dropsondes for measuring the vertical profile of mass divergence and vertical motion in the Arctic.

By integrating these objectives, this study aims to document the circle method's applicability in the Arctic environment.

Section 2 delves into the methodology, outlining how the vertical profiles of divergence and vertical velocity can be derived from horizontal wind measurements. Additionally, the airborne field campaign is introduced, along with the flight strategy adopted to test the technique. Section 3 offers the resulting vertical profiles and discusses the credibility of them along with an error analysis. Last, section 4 provides a forward-looking perspective on the implications of these measurements for future airborne campaigns.

## 2. Data and methods

### a. HALO–(AC)<sup>3</sup> campaign

The HALO–(AC)<sup>3</sup> campaign in March and April 2022 in the Norwegian sector of the Arctic was a joint effort by two collaborative programs: (i) (AC)<sup>3</sup> (Wendisch et al. 2023) and (ii) the Priority Program 1294 for the Atmospheric and Earth System Research program with HALO. Both programs are funded by the German Research Foundation [Deutsche Forschungsgemeinschaft (DFG)]. Three airborne platforms were used to probe and understand transforming air masses in the region. A Lagrangian sampling approach was adopted to track and sample air masses as efficiently and frequently as possible during their transformation (Wendisch et al. 2024). The campaign leveraged the unique capabilities of multiple distinct aircraft. This study relies on the dropsonde measurements launched by

- HALO: A long-range research aircraft operated by the German Aerospace Center [Deutsches Zentrum für Luft- und Raumfahrt (DLR)], operating from Kiruna, Sweden, as a remote sensing platform (Stevens et al. 2019). HALO conducted multiple circular flight patterns (150 km in diameter) at different locations releasing 5–10 dropsondes with even spacing along the flight path (Fig. 1). All circular flight patterns took between 35 and 45 min. The platform has an Airborne Vertical Atmospheric Profiling System (AVAPS) dropsonde system (UCAR/NCAR–Earth Observing Laboratory 1993; Hock and Franklin 1999) and uses Vaisala RD-41 sondes (Black et al. 2017).
- Polar 5 (P5) aircraft: A low-flying aircraft operated by the Alfred Wegener Institute (AWI), based in Longyearbyen, Svalbard (Wesche et al. 2016), also operated as a remote sensing platform. This aircraft conducted active and passive remote sensing measurements, focusing on investigating smaller-scale processes in the lower troposphere (at altitudes below 3–5 km). The platform operates an AVAPS Lite dropsonde system (Michaelis et al. 2022) also using Vaisala RD-41 dropsondes (Vaisala 2023).

Vaisala RD-41 dropsondes measured temperature with a resolution of 0.01°C, humidity with a resolution of 0.1% RH, and pressure with a resolution of 0.01 hPa (Vaisala 2023). The horizontal wind velocity was derived from the global positioning system (GPS) with an estimated accuracy of 0.1 m s<sup>−1</sup> (Hock and Franklin 1999; Wang et al. 2015).

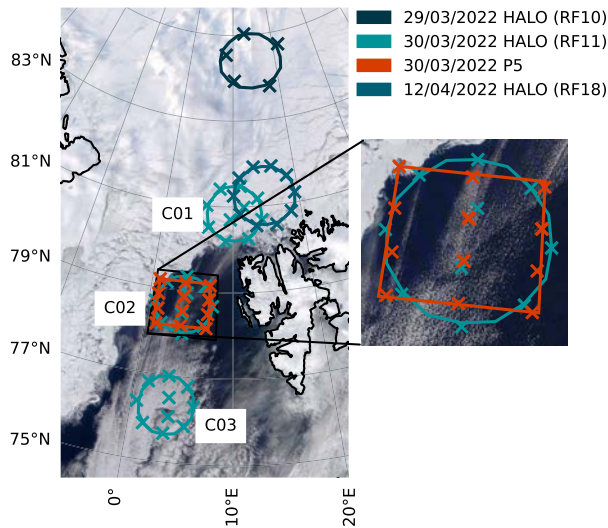


FIG. 1. HALO-(AC)<sup>3</sup> flight track patterns for three HALO flights (RF10, RF11, and RF18; blue) and P5 (red) with the locations of the dropsonde launches (x). Satellite image at the time of RF11 30 Mar 2022 from Terra MODIS (NASA 2022, Worldview Snapshots) in the background, adapted in modified form from Fig. 17a in Wendisch et al. (2024).

This study is based on three HALO-(AC)<sup>3</sup> research flights (RFs) of HALO, conducted on 29 March (RF10), 30 March (RF11), and 12 April (RF18). On all 3 days, mesoscale circles (15 km diameter) were flown west of Svalbard. Figure 1 shows their locations and a satellite image of the day of RF11 for reference. RF10 included a mesoscale horizontal circle close to the North Pole but was subject to strict airspace restrictions, by which only five dropsondes could be released. On the next day during RF11, three circles were flown (C01 north of Svalbard, C02 west of Svalbard, and C03), each situated to match the most estimated southbound Lagrangian trajectories of the air masses sampled during RF10. A total of eight dropsondes were deployed along the perimeter of each circle, and two additional sondes were released in their interior. The third flight with a circular flight pattern investigated here (RF18) featured a single circle with 10 sondes launched on its perimeter. Each HALO-(AC)<sup>3</sup> flight pattern was conducted at a height of  $\sim 8$  km and took up to 45-min time.

Notably on 30 March 2022, the Polar 5 executed a gridded flight pattern with regularly spaced dropsonde releases, collocated with HALO RF11's second mesoscale circle (RF11 C02) (Fig. 1, red) at a height of  $\sim 2.5$  km. This strategic spatial collocation of flight patterns had the aim of obtaining two independent sets of soundings for the same area, enabling a critical assessment of the divergence calculations. For operational reasons, P5 conducted its pattern 45 min after the collocated RF11, and the pattern took 3 h in total, because of a more complex flight pattern, but all dropsondes on the outer edge of the pattern were dropped within 2 h. To avoid confusion, with different numbering of the research flights of both aircraft, this flight will not be referred to by its flight number, but by the platform name (P5).

### b. Line-integral method

Given the dropsonde data, the first method for calculating divergence relies on a line integral. Vertical wind velocity in the atmosphere is related to horizontal wind divergence using the continuity equation under the incompressibility assumption. In practice, estimating the mean divergence  $D$ , and thus subsidence, of an area  $A$  is achieved by measuring the integrated horizontal velocity  $\mathbf{v}_h$  at its boundary  $\partial A$ , where  $\partial A$  is a closed curve surrounding  $A$ , according to the Gauss theorem:

$$D = \frac{1}{A} \oint_{\partial A} \mathbf{v}_h \cdot \mathbf{n} \, dl. \quad (1)$$

This is the conceptual basis behind the line-integral method, which utilizes the perimeter's closed nature of measuring horizontal wind either at flight level (Lenschow et al. 1999, 2007) or with sounding profiles (Bony and Stevens 2019). The number of observations attainable along the flight pattern is finite; therefore, it is more appropriate to write Eq. (1) in the form of a sum:

$$D = \frac{1}{A} \sum_N v \delta l, \quad (2)$$

where  $N$  is the number of dropsondes considered,  $A$  is the area enclosed by the flight track, and  $v$  is the radial component to the curve. The term  $\delta l$  represents the length element computed as  $L/N$ , where  $L$  is the length of the perimeter, assuming the sounding points are approximately uniformly distributed along the curve. The horizontal displacement of the dropsondes from the mean coordinates of their corresponding profiles during their descent is small and the sondes drift in the same direction, causing only small deformations of the pattern (see Fig. A1 in appendix A). We estimate that taking the deformation of the pattern in the vertical into account would lead to relative changes smaller than 1% and 10% in the divergence and pressure velocity signal, respectively (Fig. B1 in appendix B). For simplicity of the method, we decided to disregard the horizontal displacement of the dropsondes from the mean coordinate of their corresponding profiles for this analysis. Vertical motion, expressed from now on in terms of pressure velocity  $\omega = dp/dt$ , with the pressure  $p$ , can then be derived through the vertical integration of the  $D$  profiles over the column and accounting for the change in air density  $\rho$ :

$$\omega = -g \rho \int_0^z D \, dz, \quad (3)$$

where  $g = 9.81 \text{ m s}^{-2}$  is the gravitational acceleration.

### c. Regression method

An alternative method for calculating mesoscale divergence  $D$  makes use of its dependence on the spatial gradients in the horizontal wind field  $\mathbf{v}_h = (u, v)$ :

$$D = \nabla \cdot \mathbf{v}_h = \frac{\partial u}{\partial x} + \frac{\partial v}{\partial y}. \quad (4)$$

Under the assumption that wind fluctuations in both longitude and latitude follow a linear pattern at every vertical level  $z$ ,

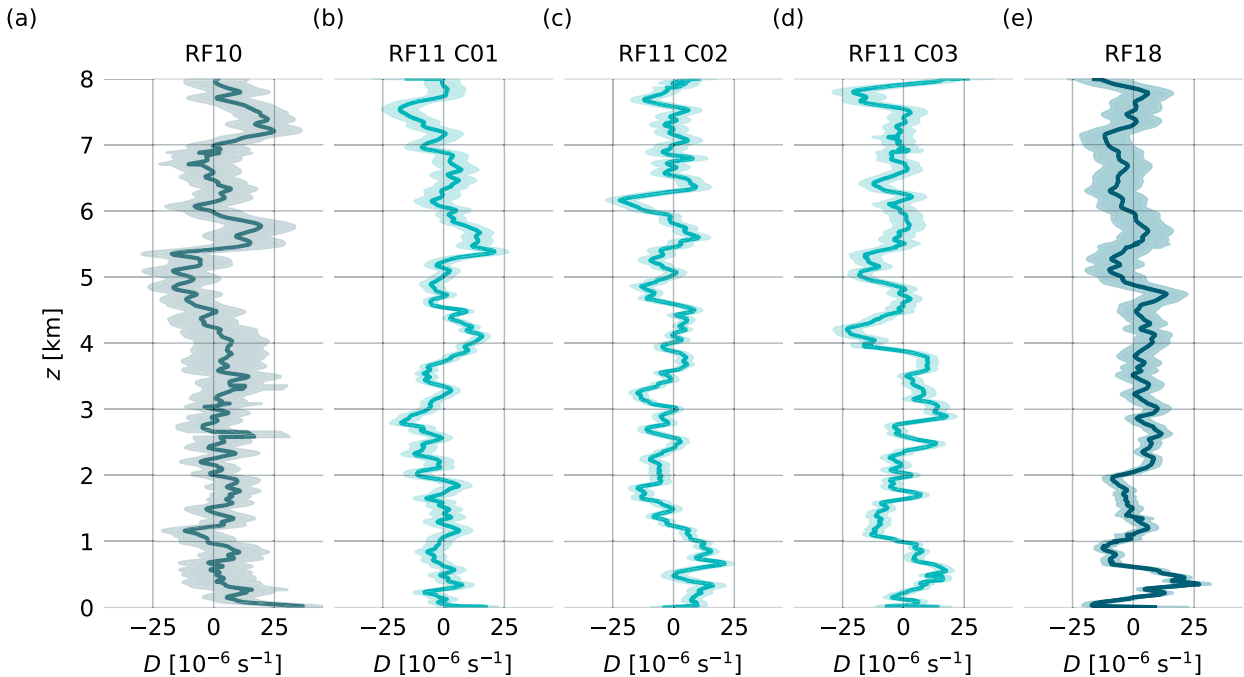


FIG. 2. Vertical profiles of wind divergence  $D$  obtained by the regression method from HALO pattern flights (a) RF10 (five sondes), (b) RF11 C01 (10 sondes), (c) RF11 C02 (10 sondes), (d) RF11 C03 (10 sondes), and (e) RF18 (10 sondes) with estimated error (shaded).

the wind at any point at the circumference can be approximated by a first-order Taylor expansion from the center point of the flight pattern (Lenschow et al. 2007):

$$\mathbf{v}_h = \mathbf{v}_{h,0} + \frac{\partial \mathbf{v}_h}{\partial x} \Delta x + \frac{\partial \mathbf{v}_h}{\partial y} \Delta y + \frac{\partial \mathbf{v}_h}{\partial t} \Delta t + \mathcal{O}(\mathbf{v}_h''), \quad (5)$$

with the mean wind velocity over all dropsondes being  $\mathbf{v}_{h,0}$ , the eastward displacement  $\Delta x$ , and the northward displacement  $\Delta y$  from the center of the circle. We can justify omitting the time dependence (stationarity) in Eq. (5) by the significant difference in aircraft speed compared to wind speed, making the sampling time scale much smaller than the advective time scale. Employing stationarity also resolves concerns arising from the nonindependence of the aircraft's time and space sampling (Bony and Stevens 2019).

Inserting measured data from deployed dropsondes into Eq. (5), after removing time derivatives and higher-order terms, yields an overdetermined linear system of equations, for which the least squares solution can be found through linear regression. Unlike the line-integral method, this method does not require a closed flight path, and it can utilize all dropsondes deployed in a constrained area during a time frame, where stationarity is justifiable (Lenschow et al. 2007).

Most previous efforts using the regression method to calculate mesoscale divergence from sonde patterns were conducted in subtropical regions (NARVAL and EUREC<sup>4</sup>A) and twice in the midlatitudes during the Aerosol Cloud Meteorology Interactions over the Western Atlantic Experiment (ACTIVATE) (Li et al. 2022). At those locations, the geographical coordinate system (latitude, longitude) can be approximated

equidistant and Cartesian coordinates  $(x, y, z)$  are appropriate to express horizontal gradients. In contrast, the HALO-(AC)<sup>3</sup> campaign target area is much closer to the North Pole, where horizontal distances associated with Cartesian coordinates from latitudes and longitudes become increasingly distorted, which would introduce substantial errors in gradient calculations.

To effectively address this problem, we introduce the regression method in a spherical coordinate system, with the distance  $r$  from Earth's center, the polar angle  $\theta$ , and the azimuth angle  $\varphi$ . This enables more accurate calculations by inherently accommodating the curvature of Earth. By applying a coordinate transformation from Cartesian to spherical coordinates (Bronshstein et al. 2007), the regression method can then be written as

$$\mathbf{v}_h = \mathbf{v}_{h,0} + \frac{\partial \mathbf{v}_h}{\partial \theta} \Delta \theta + \frac{\partial \mathbf{v}_h}{\partial \varphi} \Delta \varphi, \quad (6)$$

$$D = \nabla \cdot \mathbf{v}_h = \frac{1}{r \sin(\theta)} \left[ \frac{\partial u}{\partial \varphi} + \frac{\partial \sin(\theta)v}{\partial \theta} \right]. \quad (7)$$

### 3. Results

For all available circular flight patterns of HALO (Fig. 1), we calculated divergence as a function of altitude  $z$  up to a height of 8 km using the regression method; see Fig. 2. Of all five circles, the three central ones were flown on the same day, sampling the low-level air mass at multiple locations. The profile of RF10 (Fig. 2a) showcases the largest ranges of the estimated error, which we obtained through Gaussian error propagation of the standard errors of the wind direction

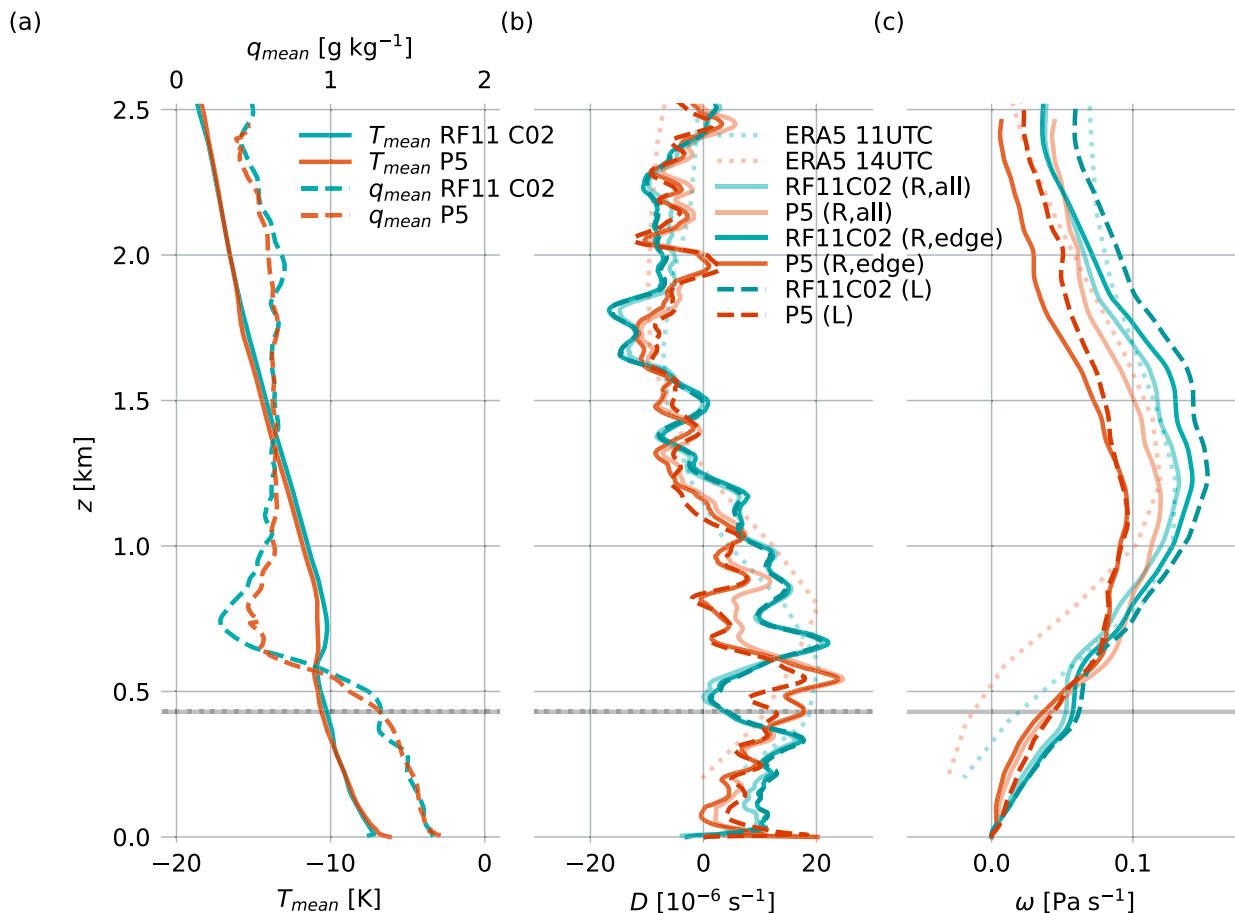


FIG. 3. Vertical profiles of the mean temperature  $T_{\text{mean}}$  and specific humidity  $q_{\text{mean}}$ , averaged over all dropsonde measurements deployed during each (a) flight, (b) mass divergence  $D$ , and (c) pressure velocity  $\omega$  obtained from dropsonde measurements from the collocated flight of HALO (RF11 C02) (blue) and P5 (red) aircraft on 30 Mar 2022. Regression method using all sondes  $R$  (all) (semitransparent), line-integral method (dashed), and regression method using only sondes which can be included in the line-integral method  $R$  (edge) (solid), mean divergence  $D$ , and pressure velocity  $\omega$  from ERA5 reanalysis (Hersbach et al. 2020) at 1100 UTC 30 Mar 2022 (approximate time of RF11 C02) and 1400 UTC (approximate time of P5), averaged over the flight areas (Figs. D1a,b), and height of the boundary layer  $h_{\text{BL}} = 0.43$  km obtained from both flights (appendix E).

and distance from the center of the flight pattern, obtained through the regression analysis (appendix C). This can be attributed to the reduced number of dropsonde launches for this specific circle (only five due to airspace restrictions). Consequently, the reduced sample size contributes to the higher error range, highlighting the potential impact of limited data on the precision of observed fluctuations.

The divergence profiles fluctuate with height around zero. Compared to the divergence profiles, sampled in the subtropics during NARVAL2 and the midlatitudes during ACTIVATE, we find a narrower range of variation ( $-25 \times 10^{-6}$  to  $25 \times 10^{-6} \text{ s}^{-1}$ ) compared to up to ( $-40 \times 10^{-6} \text{ s}^{-1}$  to  $40 \times 10^{-6} \text{ s}^{-1}$ ) in the previous campaigns (Bony and Stevens 2019; Li et al. 2022). A second characteristic is the lack of coherent features in horizontal divergence profiles in the lower layers compared to the subtropics (George et al. 2023). The divergence and convergence layers are much thinner than in the subtropics, where Bony and Stevens (2019) find layers of about 2 km, while the

observed profiles in the Arctic show smaller layers below 1 km in depth. Combined with the generally lower values of  $D$ , this could be due to the more stable atmosphere compared to the subtropics. More pronounced features in the lowest levels visible in RF11 C02, RF11 C03, and especially RF18 coincide with deeper boundary layers of 0.43, 1.04, and 0.39 km, respectively, while the boundary layer height of RF10 and RF11 C01, which were both over sea ice, is very close to the ground with 0.065 km.

To test the robustness of the horizontal circle method, and to compare the two alternatives for calculating horizontal divergence as described in section 2b, we subsequently focus on RF11 C02, before coming back to all HALO flights to study the dependence of the significance of the measurements on the number of dropsondes. The results are shown in Fig. 3, covering a shallower vertical range of up to 2.5 km, slightly below the flight height of the P5 aircraft. Zooming in on this range highlights the existence of a well-defined layer with a

marked positive divergence, peaking at about 600-m height, and allows for a more detailed comparison between the profiles from the two aircraft. Also shown are the associated vertical profiles of the pressure velocity  $\omega$ , peaking at about 1300-m height. For reference, mean profiles from the ERA5 reanalysis from the European Centre for Medium-Range Weather Forecasts (Hersbach et al. 2020), averaged over all grid points inside the sampling area (Figs. D1a,b in appendix D), are also shown, at 1100 UTC (closest time to RF11 C02) and 1400 UTC (time central within P5 flight), together with the boundary layer height calculated from the bulk Richardson number for both flights (appendix E). It needs to be noted that the dropsondes used in this study were assimilated in the ERA5 reanalysis, and therefore, this comparison is not representative of the performance of divergence and subsidence in the Arctic but is only shown as a reference to a widely used reanalysis dataset for modeling applications.

The presence of the well-defined low-level  $D$  anomaly facilitates (i) comparing the two calculation methods and (ii) assessing the robustness of the divergence measurements. It has been shown with subtropical sounding data that the line-integral method and regression method yield similar results (Bony and Stevens 2019). To revisit this question for the Arctic, we applied both methods to the collocated measurements collected by HALO and P5 on 30 March 2022. Note that the line-integral method can only be applied to sondes on the outer perimeter of the flight pattern (eight sondes for HALO and 10 sondes for P5). To achieve a fair comparison at the same statistical level, the regression method was applied to the same sondes used in the line-integral method calculation. Comparing the profiles from the regression method using all sondes to the regression method using a reduced number of sondes shows slight differences in divergence, which appear not to be accounted for when using only perimeter sondes. This suggests that deploying sondes in the center of a pattern might be beneficial. A more in-depth analysis of the statistical significance of the results using different numbers of sondes is performed later in this study.

A comparison between the results obtained from the two flight patterns (RF11 C02 and P5) reveals satisfactory alignment in divergence measurements above 1 km. However, below this level (around 500 m), a notable disparity emerges in the profiles obtained from P5 measurements, diverging significantly from those extracted from HALO data. This shift cannot be seen in the ERA5 profiles, which seem to not only capture this variability in time but only show a slight lifting of the divergence profile. The observed shift could be due to changes in the horizontal wind field during the time between the flights, affected by the island of Svalbard in the east of the measurement area, as seen in the mean wind profiles of  $u$  and  $v$  (Fig. F1 in appendix F). It is possible that these differences could be linked to lee waves, as the flight area is within the reach of the observed lee waves (see Fig. 1). The altitude of the differences in the profiles is similar to that of the Svalbard mountains, which hints at an influence of lee waves. Small changes in the flow pattern could cause shifts in the lee waves, potentially explaining the differences. However, this remains speculative, and we cannot confirm it based on our current data.

Only minor discrepancies are apparent in the divergence profiles derived from the line-integral and the regression methods with both sonde samples, indicating the potential for equal applicability of both methods. This finding confirms the results of Bony and Stevens (2019), who concluded from the similarity that the divergence measurements are not influenced by sampling errors from small-scale velocity fluctuations but are reflective of the mesoscale wind.

The pressure velocity profiles diverge with growing height as a result of the upward integration of divergence profiles including small differences. At higher altitudes, the profiles diverge even more, causing differences in the vertical velocity profiles of  $0.05$  to  $0.1 \text{ Pa s}^{-1}$  between 3 and 8 km for the RF11 C02 profile. Van der Dussen et al. (2016a) have shown that subsidence variations of similar order have a potential impact on simulated atmospheric boundary layer and cloud properties with LES of stratocumulus transitions and cannot be neglected. The divergence profiles derived from different aircraft data and methods tend to align reasonably well with the average divergence from ERA5, but the profiles at the individual grid points show high variability (Fig. D1). All dropsondes deployed during HALO RF11 (32) have been assimilated into ERA5, making a direct comparison difficult and an evaluation of ERA5 based on these results impossible. When compared to data from the ACTIVATE campaign, ERA5 profiles show less agreement and significant temporal variations in the divergence profile (Li et al. 2022), which is in line with a comparison for the other flights (Figs. D2, D3, D5, and D6), during which fewer dropsondes have been deployed and not all have been assimilated (10 out of 18 for RF10 and 5 out of 20 for RF18). However, compared to the EUREC<sup>4</sup>A campaign, ERA5 and the observations for all flights showed good agreement (George et al. 2023).

To further characterize the agreement on divergence amplitude and vertical structure between independent datasets, a correlation analysis is performed. HALO data are binned by height and correlated against P5 data for this location (Fig. 4). As the previous analysis shows similar results for the regression and the line-integral methods, the regression method will be used for the remainder of the study, as it can utilize all dropsondes and works for varying numbers of dropsondes that do not have to be arranged along a closed line. The data are classified into height bins of 50 m (about 10 data points per bin). The associated correlation coefficient is 0.734. The correlation fit is slightly tilted compared to the one-to-one line, which could be caused by small changes in the wind flow in between measurements or originate from a longer flight time of the P5 aircraft, but lies within the errors of the measurements and the fit.

As described in section 2a, we performed different flight patterns with different numbers of sondes. In accordance with the outcomes of preliminary model analyses conducted in advance of the campaign, a decision was made to employ 10 sondes for each circular flight pattern, except for RF10 for reasons of operational limitations. In the case of the rectangular flight pattern executed by P5, the strategic decision was made to launch 15 sondes to enhance spatial coverage and comprehensiveness. In Fig. 5, we present the estimated errors

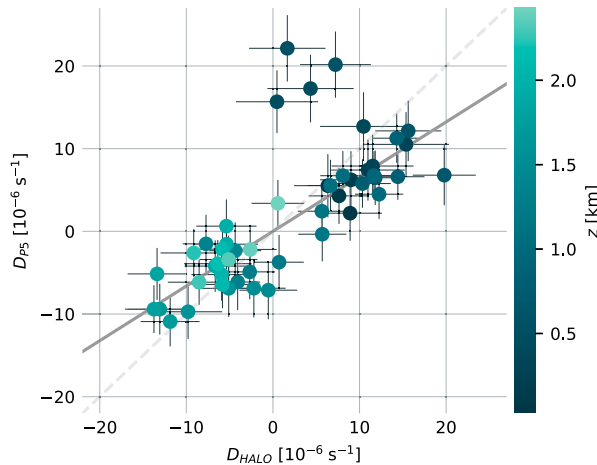


FIG. 4. Correlation between divergence profiles from HALO (RF11 C02) and P5 measurements on collocated flights for different heights (binned into bins of 50 m) (color scale) on 30 Mar 2022 obtained via regression method, correlation coefficient  $r = 0.734$  and correlation fit  $D_{PS} = (0.662 \pm 0.008 \times D_{HALO} + (7.826 \times 10^{-7} \pm 6.55 \times 10^{-13}) \text{ s}^{-1})$  (gray line), both excluding four outliers at 500 m (shaded).

resulting from the linear regression across varying quantities of sondes. This exercise aims to examine the relationship between the number of sondes and the corresponding uncertainty to obtain the optimal number of sondes required for the method with the potential to streamline costs by minimizing the number of deployed sondes while maintaining sufficiently good results for forthcoming campaigns. For each distinct flight pattern, divergence profiles were computed for every feasible combination of sondes, with a minimum threshold of five sondes. The mean vertical estimated error of all profiles sharing the same sonde count is depicted using a boxplot representation. Given the substantial similarity in results, the data from all three circles of RF11 were combined in one boxplot. Analyzing the P5 measurements, we identified a power-law relationship governing the dependence of the estimated error on the number of sondes  $N$ :

$$\overline{\text{Err}(D)} = aN^{-b} + c. \quad (8)$$

The corresponding fit parameters are shown in Table G1. The displacement of the power-law curve appears to correlate with the synoptic conditions, which were different between RF18 and RF11, with a weak cold-air outbreak present during RF10 and RF11 and a strong inversion above the surface in the lowest 500 m and Arctic cirrus on RF18. The estimated error derived from both the P5 and HALO measurements on these specific dates exhibited a notable degree of similarity. The first derivative of the fit functions for all cases reduces by 80% between  $N = 5$  and  $N = 10$  and even 85%–90% for  $N = 12$  sondes, showing a significant convergence in the estimated error of the divergence measurement. Based on the results of this analysis, we recommend using 10–12 sondes per pattern to estimate divergence on a scale of 150 km for Arctic research campaigns. This takes into account the possibility of

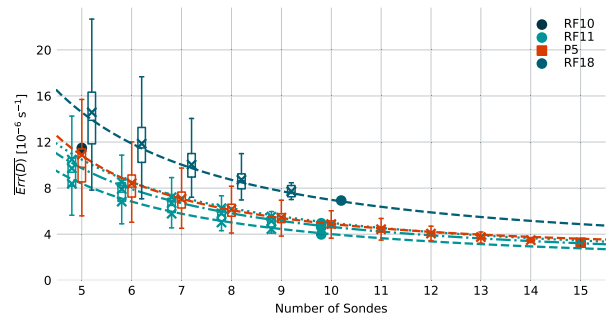


FIG. 5. Vertically averaged estimated error of divergence  $\overline{\text{Err}(D)}$  for all possible combinations of sondes  $N$  (minimum five sondes) from the regression method (boxplots, outliers not shown, RF11 and RF18 displaced for better visualization) and data from all circles of RF11 combined in one boxplot for better readability. Mean estimated error of all combinations  $x$ , estimated error for maximum number of sondes (bold marker), and power-law fit  $\Delta D = aN^{-b} + c$  for RF11 C01 (dotted), RF11 C02 (dashed), RF11 C03 (dash-dotted), RF08, and RF18; see Table G1 in appendix G for fit parameters.

sonde failures and aligns with the suggestions made by Bony and Stevens (2019) for subtropical regions.

#### 4. Conclusions

In this study, data from dropsondes launched in mesoscale synoptic situations during multiple flights of the HALO–(AC)<sup>3</sup> campaign in the Norwegian sector of the Arctic were used to calculate divergence profiles and derive mesoscale vertical velocity (subsidence). The twofold objective is to test the robustness of this method at high latitudes and to compare alternative calculation methods. The regression method and the line-integral method have demonstrated almost equivalent effectiveness at high latitudes, similar to findings from previous campaigns in the subtropics. We conclude a remarkable agreement observed in both amplitude and vertical structure of mesoscale divergence as obtained from disparate and independent sonde datasets collected by different aircraft over the same target area. Minor differences in divergence between the two datasets are likely caused by small changes in the flow between the sampling times of the two flights (approximately 45 min).

An error analysis confirms a nonlinear decrease in the estimated error  $\Delta D$  with increasing dropsonde numbers explained well by a power-law relationship, similar to results from previous studies in the subtropics. Based on these results, we recommend an optimal range of 10–12 dropsondes per mesoscale pattern, striking a balance between statistical significance and cost efficiency, while also accounting for potential sonde failures. This number could be useful for planning future airborne campaigns for measuring mesoscale divergence.

The importance of subsidence as a forcing factor for LES and single-column models (SCMs) (Mirocha and Kosović 2010; Neggers 2015; Young et al. 2018; van der Linden et al. 2019) makes this dataset relevant for future modeling

activities. LESs and SCMs are frequently used to test or develop physical parameterization schemes while requiring the prescription of a reliable representation of the mesoscale dynamics. Information about the subsidence conditions is fed into these models in the form of divergence or vertical velocity profiles that are either constructed in an idealized manner or more frequently simply acquired from reanalysis products, at times in combination with crude estimates from in situ observations. Models tend to be highly sensitive to small changes in the imposed subsidence conditions (Mirocha and Kosović 2010; van der Dussen et al. 2016b; Young et al. 2018) which calls for a more carefully considered source for this kind of forcing information. Even though the ERA5 divergence vertical profile in the area of the collocated patterns is in overall agreement with its observationally constrained counterpart—which in itself could be the result of the assimilation of the abundant dropsonde profiles available for that time period—this is not always the case. Therefore, the use of reanalysis products for forcing SCM or LES models is less than optimal. The dataset presented in this study offers a more realistic depiction of the mesoscale vertical motion, while the use of different derivation methods, flight patterns, and amounts of dropsondes provides a meaningful uncertainty range, within which the sensitivity of the models could be transparently investigated.

The results obtained in this study motivate various future research efforts. While the general circulation during the selected flights was relatively stable and slow changing, the encouraging results obtained for these conditions invite exploring different weather regimes in the Arctic further. Investigating different flight patterns and assessing the impact of nonuniformly spaced dropsondes could further facilitate the broader application of this method for flights with more diverse research objectives. Finally, expanding our knowledge on vertical motion at high latitudes furthers our general understanding of the Arctic's atmospheric dynamics and climate, could guide the coordination of future airborne campaigns in the region, and contributes to the advancement of atmospheric science in general.

*Acknowledgments.* We gratefully acknowledge the funding by the Deutsche Forschungsgemeinschaft (DFG; German Research Foundation)—Project 268020496—TRR 172, within the Transregional Collaborative Research Center “Arctic Amplification: Climate Relevant Atmospheric and Surface

Processes, and Feedback Mechanisms (AC)<sup>3</sup>.” We are further grateful for the funding of Project Grant 316646266 by the DFG (German Research Foundation) within the framework of Priority Programme SPP 1294 to promote research with HALO. We also gratefully acknowledge the funding by the DFG (German Research Foundation)—Project 442649391—Observing Local and Remote Controls on Arctic Air Mass Evolution (ORCA2). We acknowledge support from the Swedish Research Council (VR, project 2020-04064). We appreciate the financial contributions of the Alfred Wegener Institute (AWI, Bremerhaven), the German Aerospace Centre (DLR, Oberpfaffenhofen), and the Max Planck Institute for Meteorology (MPI-M, Hamburg). Pilots and technicians who have flown and operated the airplanes are thanked for all their enormous efforts. We thank Marcus Klingebiel and Davide Ori who planned and executed the research flights and the operators of the dropsonde systems Sebastian Schmidt, Imke Schirmacher, and Anja Schwarz for creating the database for this study. We acknowledge the use of imagery from the Worldview Snapshots application (<https://wvs.earthdata.nasa.gov>), part of the Earth Observing System Data and Information System (EOSDIS). ChatGPT has been used to help create the first versions of this manuscript. The authors made distinct contributions to the project. GG provided the basis for the data processing of dropsonde measurements and the regression method. FP processed the data and implemented and evaluated the regression method together with RN. MK and GS performed the line-integral method. RN, GG, and GS advised on the interpretation of the results. FP prepared the manuscript, MK wrote several sections, and RN, GS, GG, and MW revised various intermediate versions.

*Data availability statement.* The dropsondes data will be published by acceptance and can already be accessed via the (AC)<sup>3</sup> airborne module (Mech et al. 2023). The ERA5 datasets can be freely retrieved from the Copernicus Climate Change Service (C3S) Climate Data Store (CDS) at <https://cds.climate.copernicus.eu/>, last accessed on 6 November 2023. The code used to process the data is published at <https://zenodo.org/doi/10.5281/zenodo.10402060>.

## APPENDIX A

### Horizontal Displacement of Dropsondes

Figure A1 shows vertical profiles of the horizontal displacement of the dropsondes from the location of their release, to quantify the drift.

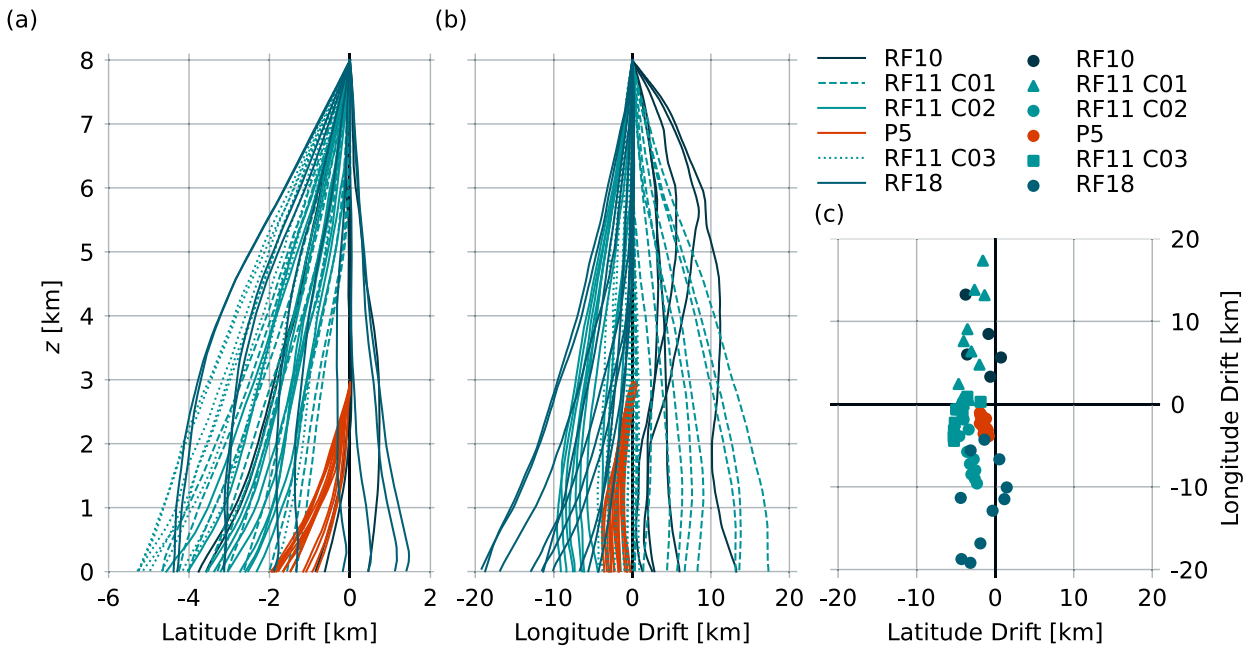


FIG. A1. Vertical profiles of horizontal displacement of dropsondes from the location of release at  $t_0$  in (a) latitude  $\text{lat} - \text{lat}(t_0)$ , (b) longitude  $\text{lon} - \text{lon}(t_0)$ , and (c) maximum horizontal displacement.

APPENDIX B

Variability in the Line-Integral Method

Figure B1 shows the relative frequency distribution of the absolute differences in the divergence and pressure velocity profiles calculated with the line-integral method, when disregarding or accounting for potential deformation of the patterns with height.

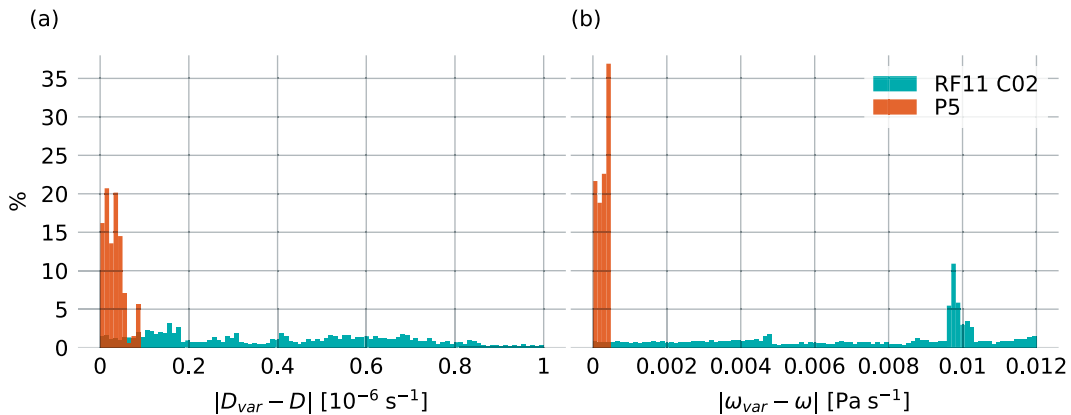


FIG. B1. Relative frequency distribution of the absolute differences in the (left) divergence and (right) pressure velocity profiles calculated with the line-integral method, when disregarding or accounting for potential pattern deformation with height ( $D, \Omega$  and  $D_{var}, \Omega_{var}$ , respectively). For the RF11 C02 flight (blue), pattern deformation includes changes in both the circle radius and relative dropsonde distances; for P5 (red), only changes in the area enclosed by the flight track are considered.

## APPENDIX C

**Error Estimation**

The error of divergence  $\text{Err}(D)$  and the error of vertical velocity  $\text{Err}(\omega)$  are obtained through Gaussian error propagation (Bronshtein et al. 2007) of the standard error of the velocity measurements and the distance from the center of the flight pattern:

$$\text{Err}[\xi(z)] = \frac{\sqrt{\sum_{k=1}^{N_{\text{Sondes}}} [\xi(z, k) - \bar{\xi}(z)]^2}}{N_{\text{Sondes}}}, \quad (\text{C1})$$

for  $\xi \in \{u, v\}$ . The error estimation of the horizontal gradient ( $\chi \in \{\theta, \phi\}$ ) is then given by

$$\text{Err}\left(\frac{\partial \xi}{\partial \chi}\right) = \frac{\text{Err}(\xi)}{\sqrt{\sum_{k=1}^{N_{\text{Sondes}}} (\chi - \bar{\chi})^2}}, \quad (\text{C2})$$

and the error on divergence  $\text{Err}(D)$  is calculated as

$$\text{Err}(D) = \frac{1}{\sin(\theta)} \sqrt{\left[\text{Err}\left(\frac{\partial u}{\partial \phi}\right)\right]^2 + \left[\text{Err}\left(\frac{\partial v}{\partial \theta}\right)\right]^2}, \quad (\text{C3})$$

and vertical velocity  $\text{Err}(\omega)$  for each height  $z_i$  is calculated as

$$\text{Err}[\omega(z_i)] = -g\bar{\rho} \int_0^{z_i} \text{Err}[D(z)] dz, \quad (\text{C4})$$

with  $g = 9.81 \text{ m s}^{-1}$  and the mean air density  $\bar{\rho}$ .

## APPENDIX D

**Profiles from Regression Method and Line-Integral Method with ERA5 for All Grid Boxes**

Figures D1–D6 show a comparison of vertical profiles of temperature and specific humidity, divergence, and pressure velocity of ERA5 to the observations with the line-integral method and the regression method for all flights.

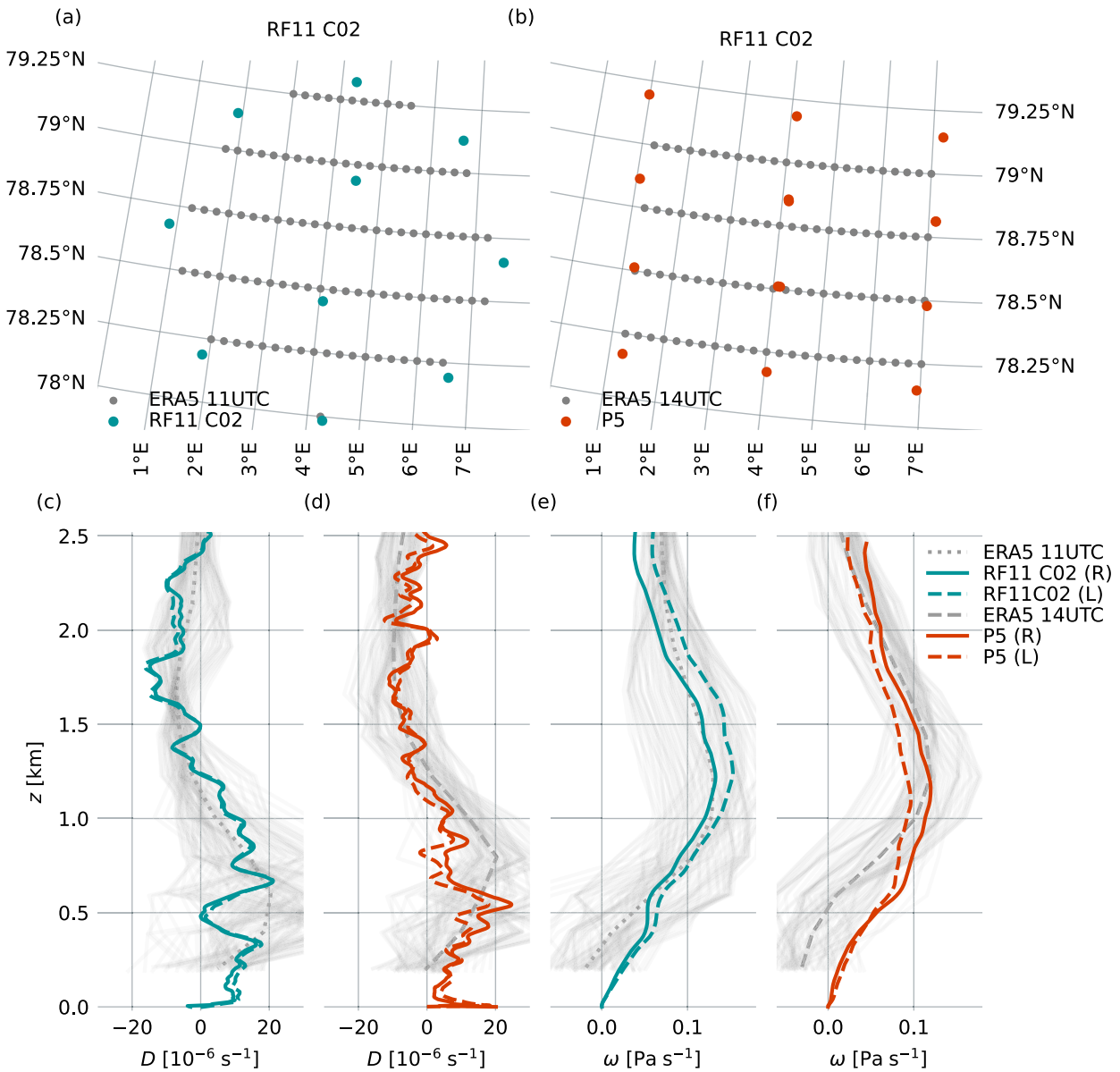


FIG. D1. Dropsonde locations of (a) RF11 C02 and (b) P5 and corresponding grid points of ERA5 [1100 UTC 30 Mar 2022 in (a) and 1400 UTC 30 Mar 2022 in (b)] inside the sampling area, vertical profiles of divergence  $D$  from (c) RF11 C02 and (d) P5 and pressure velocity  $\Omega$  from (e) RF11 C02 and (f) P5 at all grid points of ERA5 within the sampling area (light gray), averaged over all ERA5 grid points within the sampling area (black), and from dropsondes obtained with the regression method using all dropsondes [solid  $R$  (all)] and line-integral method (dashed  $L$ ).

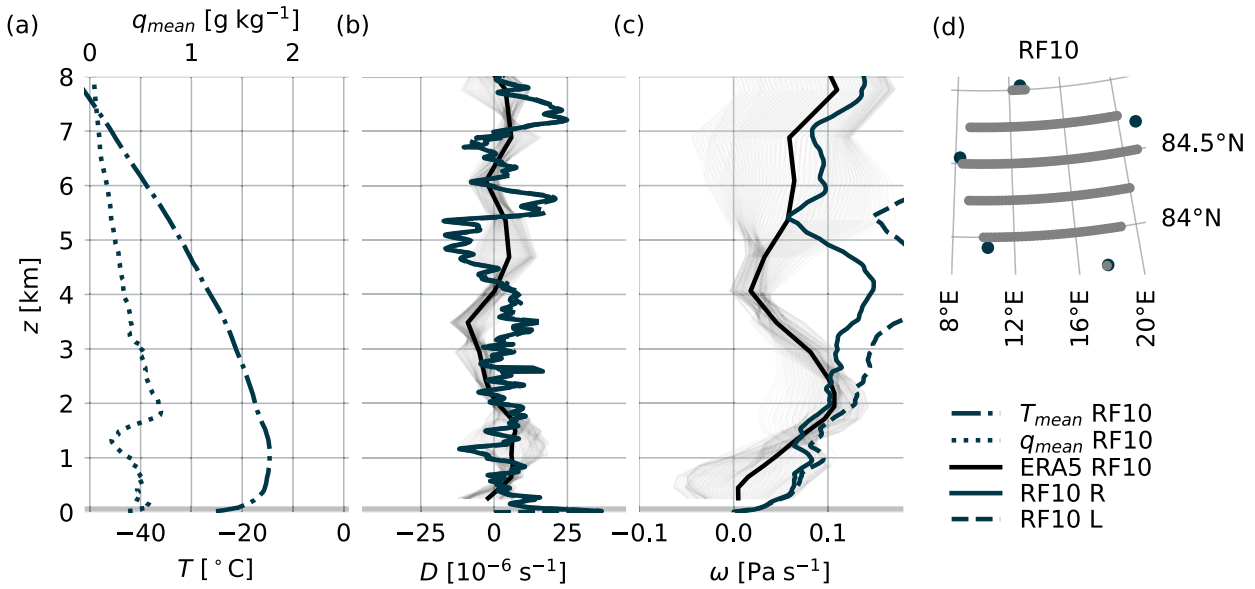


FIG. D2. (a) Vertical profiles of temperature  $T$  and specific humidity  $q$ , (b) vertical profiles of divergence  $D$ , and (c) pressure velocity  $\Omega$  at all grid points of ERA5 within the sampling area (light gray), averaged over all ERA5 grid points within the sampling area (black), and from dropsondes obtained with the regression method (blue) and line-integral method (blue, dashed), and (d) dropsonde locations of RF10 and grid points of ERA5 (1400 UTC 29 Mar 2022) inside the sampling area.

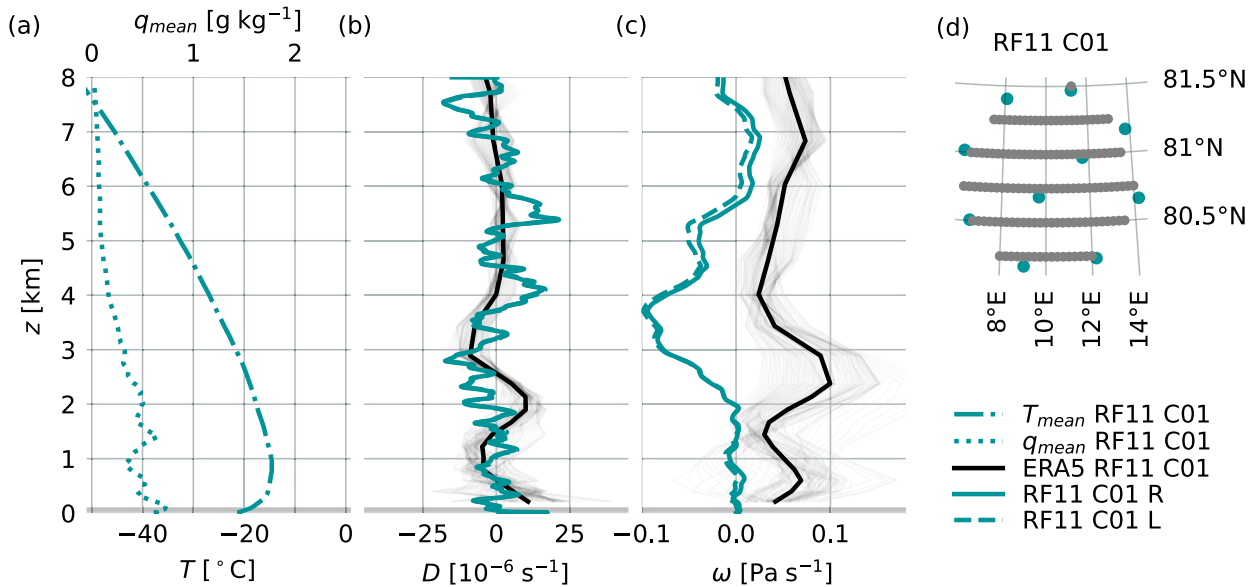


FIG. D3. (a) Vertical profiles of temperature  $T$  and specific humidity  $q$ , (b) vertical profiles of divergence  $D$ , and (c) pressure velocity  $\Omega$  at all grid points of ERA5 within the sampling area (light gray), averaged over all ERA5 grid points within the sampling area (black), and from dropsondes obtained with the regression method (blue) and line-integral method (blue, dashed), and (d) dropsonde locations of RF11 C01 and grid points of ERA5 (1000 UTC 30 Mar 2022) inside the sampling area.

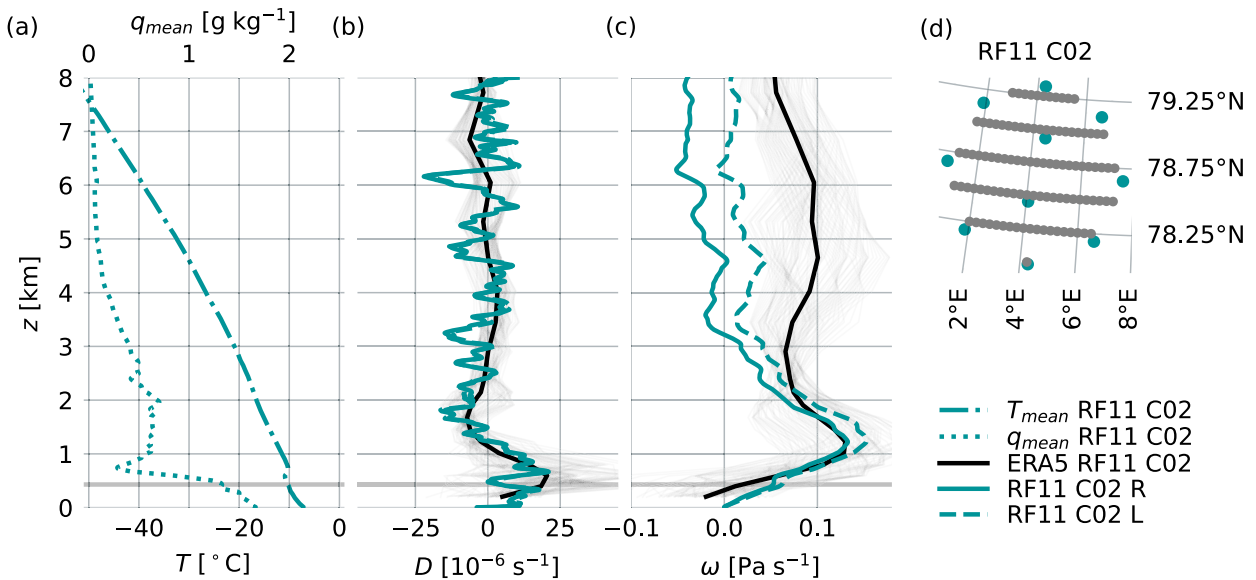


FIG. D4. (a) Vertical profiles of temperature  $T$  and specific humidity  $q$ , (b) vertical profiles of divergence  $D$ , and (c) pressure velocity  $\Omega$  at all grid points of ERA5 within the sampling area (light gray), averaged over all ERA5 grid points within the sampling area (black), and from dropsondes obtained with the regression method (blue) and line-integral method (blue, dashed), and (d) dropsonde locations of RF11 C02 and grid points of ERA5 (1100 UTC 30 Mar 2022) inside the sampling area.

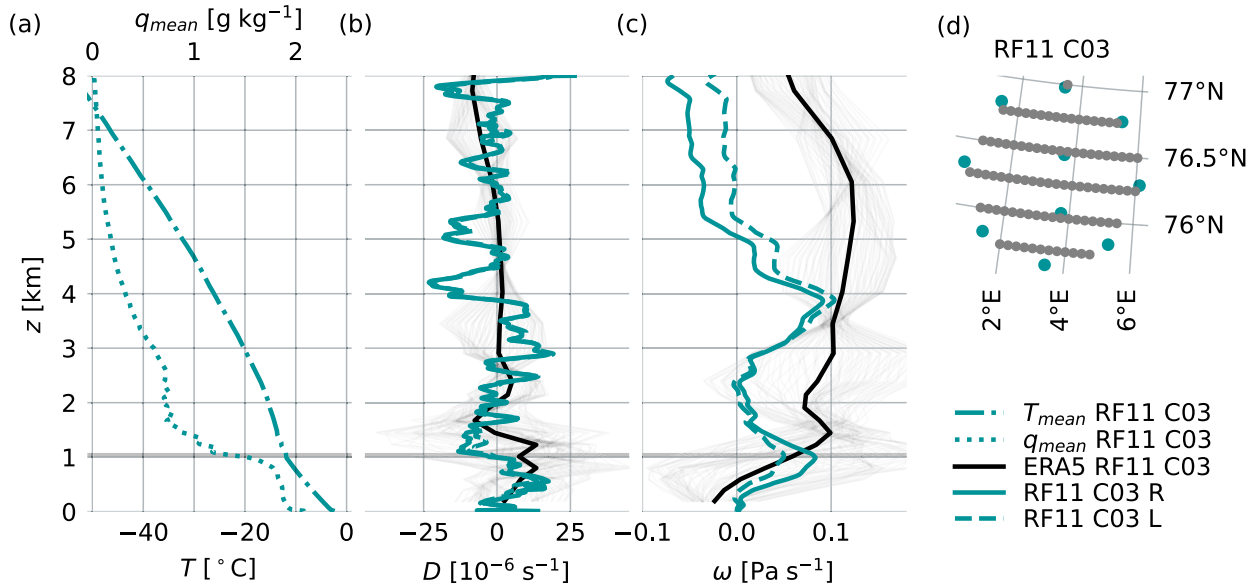


FIG. D5. (a) Vertical profiles of temperature  $T$  and specific humidity  $q$ , (b) vertical profiles of divergence  $D$ , and (c) pressure velocity  $\Omega$  at all grid points of ERA5 within the sampling area (light gray), averaged over all ERA5 grid points within the sampling area (black), and from dropsondes obtained with the regression method (blue) and line-integral method (blue, dashed), and (d) dropsonde locations of RF11 C03 and grid points of ERA5 (1200 UTC 30 Mar 2022) inside the sampling area.

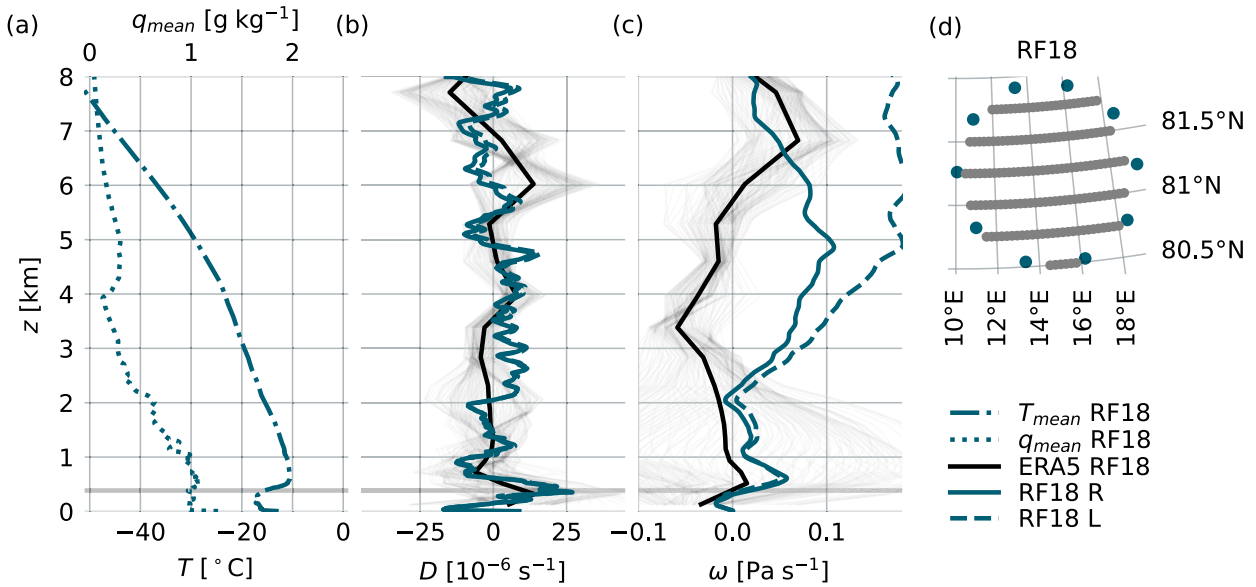


FIG. D6. (a) Vertical profiles of temperature  $T$  and specific humidity  $q$ , (b) vertical profiles of divergence  $D$ , and (c) pressure velocity  $\Omega$  at all grid points of ERA5 within the sampling area (light gray), averaged over all ERA5 grid points within the sampling area (black), and from dropsondes obtained with the regression method (blue) and line-integral method (blue, dashed), and (d) dropsonde locations of RF18 and grid points of ERA5 (1000 UTC 12 Apr 2022) inside the sampling area.

## APPENDIX E

### Boundary Layer Height Calculation

The boundary layer height  $h_{BL}$  is calculated as the height, where the bulk Richardson number  $Ri_b$  exceeds a critical threshold of  $Ri_{b,crit} = 0.25$  following the implementation in IFS CY43RL (ECMWF 2016). The moist static energy  $s_v$  is calculated for each level  $n$  as

$$s_{v,n} = C_p T_n (1 + \varepsilon q_n) + g z_n, \quad (E1)$$

with the specific heat capacity of air  $C_p = 1003 \text{ J g}^{-1} \text{ K}^{-1}$ , the temperature at each level  $T_n$  in kelvins (K), the specific humidity at each level  $q_n$ , the gravitational constant  $g = 9.81 \text{ m s}^{-2}$ , the height of each level  $z_n$  in meters (m), and  $\varepsilon = 0.61$ . Together with the squared wind velocity  $\mathbf{v} = (u, v)$  at each level,

$$|\mathbf{v}_n|^2 = u_n^2 + v_n^2, \quad (E2)$$

the bulk Richardson number  $Ri_b$  is calculated as follows:

$$Ri_{b,n} = z_n \frac{2g(s_{v,n} - s_{v,0})}{[s_n + s_0 - g(z_n + z_0)]|\mathbf{v}|^2}. \quad (E3)$$

The boundary layer height is then  $h_{BL} = z(Ri_{b,n} = Ri_{b,crit})$ .

## APPENDIX F

### Mean Profiles of Horizontal Wind

Figure F1 shows vertical profiles of the horizontal wind velocities and hodographs for the collocated flights.

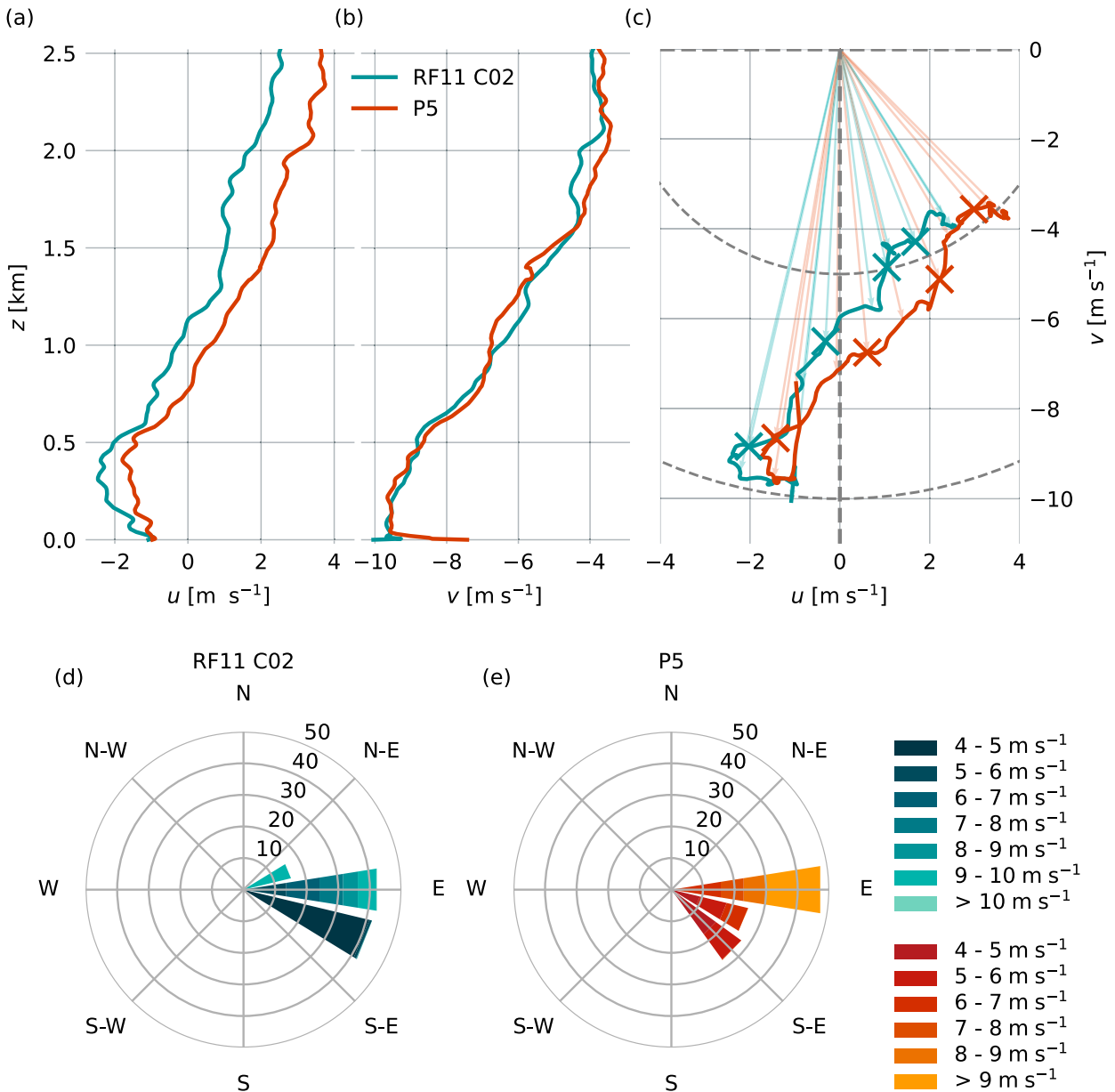


FIG. F1. Vertical profiles of horizontal wind velocities (a)  $u$  and (b)  $v$  and (c) hodograph for collocated flights RF11 C02 and P5 and wind rose plots for (d) RF11 C02 and (e) P5.

APPENDIX G

Fit Parameters of Error Statistics

Table G1 shows fit parameters of error statistics for RF11 C01, RF11 C02, RF11 C03, P5, and RF18.

TABLE G1. Fit parameters of error statistics for RF11 C01, RF11 C02, RF11 C03, P5, and RF18 (see Fig. 5), fitted to a power-law function for the estimated error of divergence  $D$ :  $\text{Err}(D) = a(1/N^b) + c$ , where  $N$  is the number of sondes and  $a$ ,  $b$ , and  $c$  are the fit parameters.

Flight	$a$ ( $10^{-6} \text{ s}^{-1}$ )	$b$	$c$ ( $10^{-6} \text{ s}^{-1}$ )
RF11 C01	$74.64 \pm 1673.96$	$1.30 \pm 0.29$	$1.21 \pm 8.84$
RF11 C02	$59.15 \pm 680.22$	$1.29 \pm 0.19$	$0.98 \pm 3.72$
RF11 C03	$69.37 \pm 994.72$	$1.30 \pm 0.20$	$1.15 \pm 5.16$
P5	$139.08 \pm 385.05$	$1.74 \pm 0.01$	$2.35 \pm 0.08$
RF18	$105.75 \pm 6536.18$	$1.32 \pm 0.55$	$1.88 \pm 30.32$

## REFERENCES

- Black, P., L. Harrison, M. Beaubien, R. Bluth, R. Woods, A. Penny, R. W. Smith, and J. D. Doyle, 2017: High-Definition Sounding System (HDSS) for atmospheric profiling. *J. Atmos. Oceanic Technol.*, **34**, 777–796, <https://doi.org/10.1175/JTECH-D-14-00210.1>.
- Bony, S., and B. Stevens, 2019: Measuring area-averaged vertical motions with dropsondes. *J. Atmos. Sci.*, **76**, 767–783, <https://doi.org/10.1175/JAS-D-18-0141.1>.
- Bronstein, I. N., K. A. Semendyaev, G. Musiol, and H. Muehlig, 2007: *Handbook of Mathematics*. 5th ed. Springer, 1164 pp., <https://ebookcentral.proquest.com/lib/kxp/detail.action?docID=645334>.
- ECMWF, 2016: IFS documentation CY43R1 - Part IV: Physical processes—IFS documentation CY43R1. European Centre for Medium-Range Weather Forecasts Tech. Doc., 223 pp., <https://ecmwf.int/en/elibrary/79989-ifs-documentation-cy43r1-part-iv-physical-processes>.
- George, G., and Coauthors, 2021: JOANNE: Joint dropsonde observations of the atmosphere in tropical North Atlantic meso-scale Environments. *Earth Syst. Sci. Data*, **13**, 5253–5272, <https://doi.org/10.5194/essd-13-5253-2021>.
- , B. Stevens, S. Bony, R. Vogel, and A. K. Naumann, 2023: Widespread shallow mesoscale circulations observed in the trades. *Nat. Geosci.*, **16**, 584–589, <https://doi.org/10.1038/s41561-023-01215-1>.
- Hersbach, H., and Coauthors, 2020: The ERA5 global reanalysis. *Quart. J. Roy. Meteor. Soc.*, **146**, 1999–2049, <https://doi.org/10.1002/qj.3803>.
- Hock, T. F., and J. L. Franklin, 1999: The NCAR GPS dropwindsonde. *Bull. Amer. Meteor. Soc.*, **80**, 407–420, [https://doi.org/10.1175/1520-0477\(1999\)080<0407:TNGD>2.0.CO;2](https://doi.org/10.1175/1520-0477(1999)080<0407:TNGD>2.0.CO;2).
- Lenschow, D. H., P. B. Krummel, and S. T. Siems, 1999: Measuring entrainment, divergence, and vorticity on the mesoscale from aircraft. *J. Atmos. Oceanic Technol.*, **16**, 1384–1400, [https://doi.org/10.1175/1520-0426\(1999\)016<1384:MEDAVO>2.0.CO;2](https://doi.org/10.1175/1520-0426(1999)016<1384:MEDAVO>2.0.CO;2).
- , V. Savic-Jovicic, and B. Stevens, 2007: Divergence and vorticity from aircraft air motion measurements. *J. Atmos. Oceanic Technol.*, **24**, 2062–2072, <https://doi.org/10.1175/2007JTECHA940.1>.
- Li, Q., M. Rapp, G. Stober, and R. Latteck, 2018: High-resolution vertical velocities and their power spectrum observed with the MAARSY radar—Part 1: Frequency spectrum. *Ann. Geophys.*, **36**, 577–586, <https://doi.org/10.5194/angeo-36-577-2018>.
- Li, X.-Y., and Coauthors, 2022: Large-eddy simulations of marine boundary layer clouds associated with cold-air outbreaks during the activate campaign. Part I: Case setup and sensitivities to large-scale forcings. *J. Atmos. Sci.*, **79**, 73–100, <https://doi.org/10.1175/JAS-D-21-0123.1>.
- Mapes, B. E., and J. Lin, 2005: Doppler radar observations of mesoscale wind divergence in regions of tropical convection. *Mon. Wea. Rev.*, **133**, 1808–1824, <https://doi.org/10.1175/MWR2941.1>.
- , P. E. Ciesielski, and R. H. Johnson, 2003: Sampling errors in rawinsonde-array budgets. *J. Atmos. Sci.*, **60**, 2697–2714, [https://doi.org/10.1175/1520-0469\(2003\)060%3C2697:SEIRB%3E2.0.CO;2](https://doi.org/10.1175/1520-0469(2003)060%3C2697:SEIRB%3E2.0.CO;2).
- Mech, M., and Coauthors, 2023: Publisher Correction: MOSAiC-ACA and AFLUX - Arctic airborne campaigns characterizing the exit area of MOSAiC. *Sci. Data*, **10**, 116, <https://doi.org/10.1038/s41597-023-02039-9>.
- Michaelis, J., A. U. Schmitt, C. Lüpkes, J. Hartmann, G. Birnbaum, and T. Vihma, 2022: Observations of marine cold-air outbreaks: A comprehensive data set of airborne and dropsonde measurements from the Springtime Atmospheric Boundary Layer Experiment (STABLE). *Earth Syst. Sci. Data*, **14**, 1621–1637, <https://doi.org/10.5194/essd-14-1621-2022>.
- Mirocha, J. D., and B. Kosović, 2010: A large-eddy simulation study of the influence of subsidence on the stably stratified atmospheric boundary layer. *Bound.-Layer Meteor.*, **134**, 1–21, <https://doi.org/10.1007/s10546-009-9449-4>.
- NASA, 2022: Worldview Snapshots. Accessed 29 September 2022, <https://wvs.earthdata.nasa.gov>.
- Neggers, R. A. J., 2015: Attributing the behavior of low-level clouds in large-scale models to subgrid-scale parameterizations. *J. Adv. Model. Earth Syst.*, **7**, 2029–2043, <https://doi.org/10.1002/2015MS000503>.
- , J. Chylik, U. Egerer, H. Griesche, V. Schemann, P. Seifert, H. Siebert, and A. Macke, 2019: Local and remote controls on Arctic mixed-layer evolution. *J. Adv. Model. Earth Syst.*, **11**, 2214–2237, <https://doi.org/10.1029/2019MS001671>.
- Stevens, B., and Coauthors, 2019: A High-Altitude Long-Range Aircraft configured as a cloud observatory: The NARVAL expeditions. *Bull. Amer. Meteor. Soc.*, **100**, 1061–1077, <https://doi.org/10.1175/BAMS-D-18-0198.1>.
- , and Coauthors, 2021: EUREC<sup>4</sup>A. *Earth Syst. Sci. Data*, **13**, 4067–4119, <https://doi.org/10.5194/essd-13-4067-2021>.
- UCAR/NCAR - Earth Observing Laboratory, 1993: NCAR Airborne Vertical Atmospheric Profiling System (AVAPS). UCAR/NCAR - Earth Observing Laboratory, <https://doi.org/10.5065/D66W9848>.
- Vaisala, 2023: Vaisala Radiosonde RD41 datasheet (in English). NCAR Tech. Doc. B212680EN-A, 2 pp., <https://docs.vaisala.com/v/u/B212680EN-A/en-US>.
- van der Dussen, J. J., S. R. de Roode, and A. P. Siebesma, 2016a: How large-scale subsidence affects stratocumulus transitions. *Atmos. Chem. Phys.*, **16**, 691–701, <https://doi.org/10.5194/acp-16-691-2016>.
- , —, and —, 2016b: How large-scale subsidence affects stratocumulus transitions. *Atmos. Chem. Phys.*, **16**, 691–701, <https://doi.org/10.5194/acp-16-691-2016>.
- van der Linden, S. J. A., and Coauthors, 2019: Large-eddy simulations of the steady wintertime Antarctic boundary layer. *Bound.-Layer Meteor.*, **173**, 165–192, <https://doi.org/10.1007/s10546-019-00461-4>.
- Wang, J., and Coauthors, 2015: A long-term, high-quality, high-vertical-resolution GPS dropsonde dataset for hurricane and other studies. *Bull. Amer. Meteor. Soc.*, **96**, 961–973, <https://doi.org/10.1175/BAMS-D-13-00203.1>.
- Wendisch, M., D. Handorf, I. Tegen, R. A. J. Neggers, and G. Spreen, 2021: Glimpsing the ins and outs of the Arctic atmospheric cauldron. *Eos*, **102**, <https://doi.org/10.1029/2021EO155959>.
- , and Coauthors, 2023: Atmospheric and surface processes, and feedback mechanisms determining Arctic amplification: A review of first results and prospects of the (AC)<sup>3</sup> project. *Bull. Amer. Meteor. Soc.*, **104**, E208–E242, <https://doi.org/10.1175/BAMS-D-21-0218.1>.

- , and Coauthors, 2024: Overview: Quasi-Lagrangian observations of Arctic air mass transformations—Introduction and initial results of the HALO-(AC)<sup>3</sup> aircraft campaign. *Atmos. Chem. Phys.*, **24**, 8865–8892, <https://doi.org/10.5194/acp-24-8865-2024>.
- Wesche, C., D. Steinhage, and U. Nixdorf, 2016: Polar aircraft Polar5 and Polar6 operated by the Alfred Wegener Institute. *J. Large-Scale Res. Facil.*, **2**, A87, <http://doi.org/10.17815/jlsrf-2-153>.
- Young, G., P. J. Connolly, C. Dearden, and T. W. Choullarton, 2018: Relating large-scale subsidence to convection development in Arctic mixed-phase marine stratocumulus. *Atmos. Chem. Phys.*, **18**, 1475–1494, <https://doi.org/10.5194/acp-18-1475-2018>.